

Modelling Miniature Incandescent Light Bulbs for Thermal Infrared ‘THz Torch’ Applications

Fangjing Hu · Stepan Lucyszyn

Received: 26 September 2014 / Accepted: 10 December 2014 /

Published online: 14 January 2015

© The Author(s) 2015. This article is published with open access at Springerlink.com

Abstract The ‘THz Torch’ concept is an emerging technology that was recently introduced by the authors for implementing secure wireless communications over short distances within the thermal infrared (20–100 THz, 15 μm to 3 μm). In order to predict the band-limited output radiated power from ‘THz Torch’ transmitters, for the first time, this paper reports on a detailed investigation into the radiation mechanisms associated with the basic thermal transducer. We demonstrate how both primary and secondary sources of radiation emitted from miniature incandescent light bulbs contribute to the total band-limited output power. The former is generated by the heated tungsten filament within the bulb, while the latter is due to the increased temperature of its glass envelope. Using analytical thermodynamic modelling, the band-limited output radiated power is calculated, showing good agreement with experimental results. Finally, the output radiated power to input DC power conversion efficiency for this transducer is determined, as a function of bias current and operation within different spectral ranges. This modelling approach can serve as an invaluable tool for engineering solutions that can achieve optimal performances with both single and multi-channel ‘THz Torch’ systems.

Keywords THz Torch · thermal infrared · thermodynamics · band-limited blackbody source

1 Introduction

The thermal infrared frequency bands, from 20 to 40 THz (15 μm to 7.5 μm) and 60 to 100 THz (5 μm to 3 μm), are best known for applications in thermography. There has been little in the way of enabling technologies within this part of the electromagnetic spectrum to support wireless communications. However, this largely unused spectral range offers opportunities for the development of secure communications. To this end, the ‘THz Torch’ concept was recently introduced by the authors [1–6]. The ‘THz Torch’ technology fundamentally exploits engineered blackbody radiation, by partitioning thermally-generated noise power into pre-

F. Hu · S. Lucyszyn

Centre for Terahertz Science and Engineering, Imperial College London, Exhibition Road, London SW7 2AZ, UK

F. Hu · S. Lucyszyn (✉)

Optical and Semiconductor Devices Group, Department of EEE, Imperial College London, Exhibition Road, London SW7 2AZ, UK

e-mail: s.lucyszyn@imperial.ac.uk

defined frequency channels. The band-limited power in each channel is then independently pulsed-modulated, transmitted and detected, creating a robust form of short-range secure communications in the thermal infrared. In this paper, the radiation mechanisms associated with the basic transducer within the '*THz Torch*' transmitter will be investigated, leading to the calculation of output radiated power and then output radiated power to input DC power conversion efficiency for this transducer.

The first incandescent light bulb to employ a tungsten filament was patented in 1904 by Just and Hanaman [7], offering greater luminosity in the visible spectrum, when compared to carbon filaments. Since then, a great deal of research has been undertaken to investigate the optical, electrical, chemical and thermal properties of tungsten materials; as well as the characteristics of tungsten light bulbs [8–14]. More recently, due to advances in materials and nanotechnology, higher luminous efficiency has been achieved by improving the emissivity of the filaments or reducing the infrared radiation contribution to the blackbody spectrum without reducing the radiation at visible wavelengths [15–17].

With traditional incandescent light bulb applications, only output radiated power within the visible spectrum is considered useful, while the remaining energy is considered to be lost. This explains why they are highly inefficient when compared to white light-emitting diodes (LEDs). Fortunately, these bulbs represent a low cost far/mid-infrared thermal source, which has been exploited by the authors to implement secure short range wireless communications. However, for the thermal infrared, the modelling approaches used for the visible spectral range is insufficient for predicting the band-limited output power from incandescent light bulbs. Therefore, an analytical thermodynamic modelling approach needs to be developed, so that the performance of both single and multi-channel '*THz Torch*' thermal infrared systems can be optimised.

In the thermal infrared, technologies have also been developed to improve the emission efficiency of thermal sources at specific wavelengths by modifying the blackbody radiation using periodic microstructures [18–22]. However, most of these studies are based on sophisticated and time-consuming technologies, such as electron beam lithography or a repetitive etching-and-deposition process [17]. Therefore, these devices cannot be easily mass produced. Most of the thermal infrared sources on the market still rely on *untrimmed* blackbody radiation using materials with high emissivity. It should be noted that although such thermal-based sources offer many benefits (e.g., simplicity, ease of tuning and affordability), the main drawback is that there is no signal coherency, as with all unmodulated noise sources. Thus, only the intensity of band-limited output power can be controlled.

For the simple proof-of-concept demonstrator, the '*THz Torch*' transmitter consists of five Eiko 8666-40984 miniature incandescent light bulbs, having a length of 6.3 mm and diameter 2.6 mm [1–6]. These bulbs are connected in series and assembled into a compact cylindrical package having an outer diameter of 8.2 mm, as shown in Fig. 1. In the thermal infrared, such commercial-off-the-shelf (COTS) bulbs are not perfect blackbody radiators (since their tungsten filaments have low emissivity), their windows have relatively poor transmission characteristics (due to the high absorption and reflectance of the glass envelopes) and without an additional collimating lens and back reflector the spreading loss is high. Nevertheless, these COTS transducers offer a very low cost means of converting input electrical power into output thermal infrared radiation.

The thermal analysis of incandescent light bulbs involves all three fundamental methods of heat transfer: radiation, conduction and convection. This analysis is inherently complex, as it requires the study of a number of interacting mechanisms: (a) primary radiation from the filament (which appears mostly in the frequency spectrum between millimeter-wave and beyond visible); (b) absorption of primary radiation by the glass envelope, causing it to heat

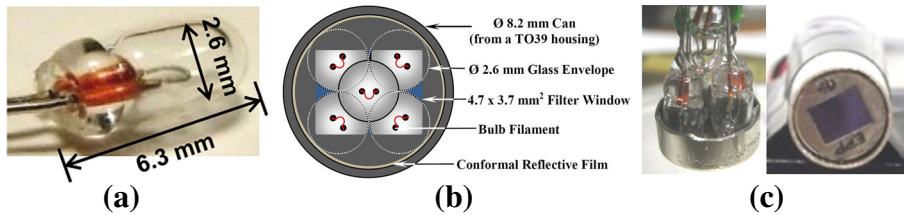


Fig. 1 ‘THz Torch’ transmitter transducers [1–6]. (a) photograph of a single incandescent light bulb; (b) illustration of basic assembly; (c) final assembly (left: internal view showing the 5-bulb arrangement; right: external view of the THz band-pass filter)

up; (c) thermal convection inside the glass envelope, causing the filament to heat up the glass envelope; (d) thermal conduction within the glass envelope and also within the two electrical leads to the outside world, which act as poor heat sinks; (e) secondary radiation from the glass envelope (which appears mostly in the thermal infrared spectral region, due to a much lower outside surface temperature); (f) thermal conduction from the glass envelope to the contacting environments on both sides; and (g) thermal convection outside the glass envelope. Due to this inherent complexity, it is not possible to individually quantify the effects of all the mechanisms.

The output radiated power contributed by the primary source of radiation lies in the spectral region dominated by high transmittance through the glass envelope; while that from secondary radiation lies in the spectral region dominated by high absorptance within the glass envelope. The power transmittance for typical (soda lime silica) window glass will first be calculated, and the band-limited output radiant intensity due to primary radiation will be determined. Then, the outside surface temperature of the glass envelope will be measured directly and the band-limited output radiant intensity due to secondary radiation will be determined. The combined band-limited output radiated power is then measured, using a calibrated thermal detector, which verifies our modelling of the two radiation sources for this basic transducer.

2 Primary Radiation Modelling

Primary radiation is defined as the output power that is generated directly from the tungsten filament and passes through the glass envelope. When a bias electrical current is applied, the temperature of the filament increases, due to Joule heating. In theory, the filament will radiate electromagnetic energy across the whole frequency spectrum. An inert gas (e.g., argon) is normally used to fill the inside of the bulb; to prevent the tungsten filament from oxidizing, which would otherwise result in the catastrophic failure of the transducer.

2.1 Filament Working Temperature Estimation

One of the most important parameters of the thermal source is the working temperature of the bulb’s filament radiator. The ideal spectral radiance, as a function of wavelength, can be calculated using Planck’s law if the temperature of the radiator is known. In theory, the working temperature of the filament cannot be measured directly with the use of a calibrated thermal camera, due to the presence of the glass envelope. An alternative, widely used indirect approach is to measure the resistance of the filament, since this is a function of its working

temperature. It is not possible to ascertain the exact geometry of the filament within commercial bulbs. However, to a good degree of approximation, it can be assumed to be perfectly cylindrical, having a uniform cross-sectional area CSA [cm^2] and length l [cm]. The electrical resistivity of tungsten $\rho(T)$, as a function of absolute temperature T , can be expressed in terms of the filament resistance $R(T)$:

$$\rho(T) = R(T) \cdot (CSA/l)_{\text{eff}} \quad [\Omega \cdot \text{cm}] \quad (1)$$

Measured data [23] for the resistivity of tungsten $\rho(T)$ against temperature, shown in Fig. 2, can be accurately modelled by the following empirical quadratic expression

$$\rho(T) = 2.228 \times 10^{-8} \cdot T^2 + 2.472 \times 10^{-4} \cdot T - 1.859 \times 10^{-2} [\Omega \cdot \mu\text{m}] \quad (2)$$

for $600 < T$ [K] $< 3,000$

At room temperature, $\rho(288 \text{ K}) = 5.14 \times 10^{-6} \Omega \cdot \text{cm}$ [23]. The combined resistance of five Eiko 8666-40984 bulbs connected in series is directly measured to be 23.6Ω at room temperature. Therefore, if the parasitic resistances of the short electrical leads are considered negligible (which is a good assumption), this gives an average value of $R(288 \text{ K}) = 4.72 \Omega$ for each bulb filament. As a result, the effective ratio of cross-sectional area to length can be extracted using (1) and (2), to give a value of $(CSA/l)_{\text{eff}} = 10.9 \text{ nm}$, which is assumed to be temperature independent. By indirectly measuring the resistance of a bulb, at a specific bias current, the working temperature can now be estimated to an acceptable degree of accuracy.

2.2 Ideal Spectral Radiance Estimation

After estimating the working temperature of the bulb filament radiator, the ideal (i.e. black-body) spectral radiance $I_{BB}(\lambda, T)$ can be obtained by applying Planck's law, to give

$$I_{BB}(\lambda, T) = \frac{2hc^2}{\lambda^5} \cdot \frac{1}{e^{hc/\lambda k_B T} - 1} \quad [\text{W}/\text{m}^2/\text{sr}/\text{m}] \quad \text{having a spectral peak at } \lambda_{\text{peak}} = \frac{b}{T} [\text{m}] \quad (3)$$

where $I_{BB}(\lambda, T)$ is the power radiated per unit area of emitting surface in the normal direction per unit solid angle per unit wavelength at the absolute temperature T for the blackbody radiator; λ is the free space wavelength; h is the Planck constant; c is the speed of light in a vacuum; k_B is the Boltzmann constant; and b is Wien's displacement constant. Fig. 3(a) shows the ideal spectral radiance against wavelength at different temperatures.

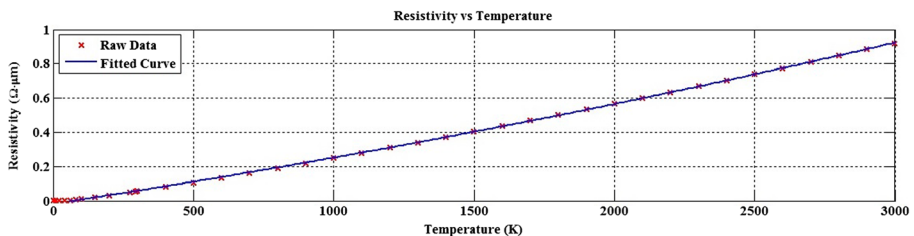


Fig. 2 Empirical curve fit of measured resistivity of tungsten against temperature [4]

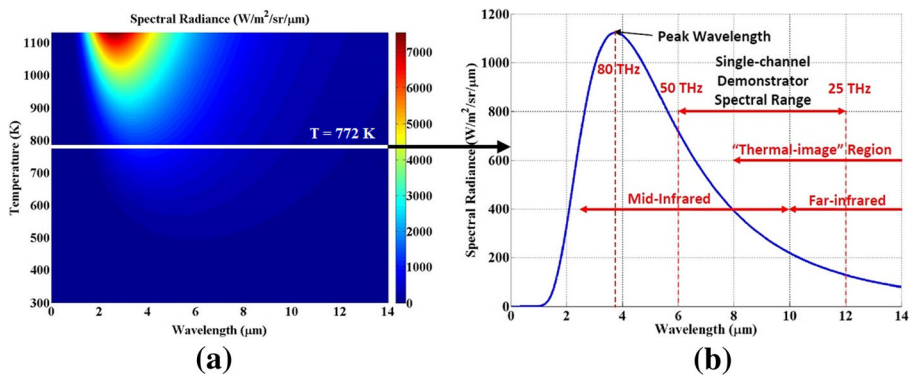


Fig. 3 Calculated ideal spectral radiance versus wavelength at (a) various temperatures; (b) an example working temperature of 772 K

In practice, the emissivity $\varepsilon(\lambda, T)$ of the emitter must be included. If the ambient temperature is assumed to be T_0 [K], the net spectral radiance emanating from the radiator is given by

$$I_{NET}(\lambda, T) = \varepsilon(\lambda, T) \cdot \left(\frac{2h c^2}{\lambda^5} \cdot \frac{1}{e^{hc/\lambda k_B T} - 1} - \frac{2h c^2}{\lambda^5} \cdot \frac{1}{e^{hc/\lambda k_B T_0} - 1} \right) \quad [\text{W/m}^2/\text{sr/m}] \quad (4)$$

With the earliest experiments, the Eiko 8666-40984 bulbs had a quiescent DC biasing current of 44 mA, which gives an estimated filament working temperature of 772 K and a corresponding spectral radiance peak at 80 THz (3.75 μm), as shown in Fig. 3(b). This peak frequency can be easily adjusted by changing the bias current. With a larger bias current, one can obtain higher spectral radiance levels, yielding an increased integrated output power for transmission. However, the penalty for this is a decrease in the band-limited output radiated power to input DC power conversion efficiency for this transducer; which may be an issue where available DC supply power is at a premium (e.g., coin battery powered security key fob applications).

Taking the effective radiating area of the radiator into account and then integrating over the spectral band of interest, the band-limited net output radiant intensity can be expressed as

$$I(T) = A_{eff} \cdot \int_{\lambda_2}^{\lambda_1} I_{NET}(\lambda, T) \, d\lambda \quad [\text{W/sr}] \quad (5)$$

where A_{eff} [m^2] is the total effective radiating area of the radiator; and λ_1 and λ_2 are the free space wavelengths associated with the lower and upper frequencies of interest, respectively.

2.3 Bulb Filament Emissivity Estimation

Most materials are far from being the perfect blackbody radiator. As a result, they are not efficient at emitting blackbody radiation. Emissivity $\varepsilon(\lambda, T)$, defined as the ratio of energy radiated by a material to that radiated by an ideal blackbody at the same wavelength and temperature, is a parameter that characterises this efficiency. In practice, if the spectral range is not too large, the emissivity at the surface of a material is only a function of

temperature (to a good approximation). Measured data [23] for the spectrum-average emissivity of tungsten $\overline{\varepsilon_{\text{filament}}}(T_{\text{filament}})$, shown in Fig. 4, can be accurately modelled by the following linear expression

$$\overline{\varepsilon_{\text{filament}}}(T_{\text{filament}}) \approx 1.343 \times 10^{-4} \cdot T - 2.019 \times 10^{-2} \quad (6)$$

2.4 Band-limited Radiant Intensity from Primary Radiation

According to (5), the radiant intensity from the primary source of radiation can be expressed as

$$I_{\text{primary}}(T_{\text{filament}}) = I_{\text{filament}}(T_{\text{filament}}) \text{ [W/sr]} \quad (7)$$

with

$$I_{\text{filament}}(T_{\text{filament}}) = A_{\text{eff_filament}} \cdot \int_{\lambda_2}^{\lambda_1} T_G(\lambda) \cdot I_{\text{NET}}(\lambda, T_{\text{filament}}) d\lambda \text{ [W/sr]} \quad (8)$$

where T_{filament} represents the working temperature for all identical filaments, extracted after determining the filament's resistance; $A_{\text{eff_filament}} = A_{\text{filament}}/2 \text{ [m}^2\text{]}$ is the estimated total effective radiating area (which assumes that only radiation in the outward direction is considered) for all five filaments, if the total radiant intensity for the 5-bulb array is required; $T_G(\lambda)$ is the power transmittance of the glass envelope; and $I_{\text{NET}}(\lambda, T_{\text{filament}})$ is the net spectral radiance of the filament at T_{filament} .

In order to calculate (8), $T_G(\lambda)$ and $A_{\text{eff_filament}}$ first have to be obtained. With the former, the inert gas within the glass envelope is assumed to be air (which is a good assumption); resulting in air-glass and glass-air boundaries. This problem can be represented by an analogous 2-port network (adapted from [24]), as illustrated in Fig. 5. Here, \hat{P}_i , \hat{P}_r , \hat{P}_a and \hat{P}_t represent the incident, reflected, absorbed and transmitted power of the associated electromagnetic waves, respectively. Within the glass, the propagation constant $\gamma = \alpha + j\beta$, where α is the attenuation constant and β is the phase constant; and T_h is the thickness of the glass.

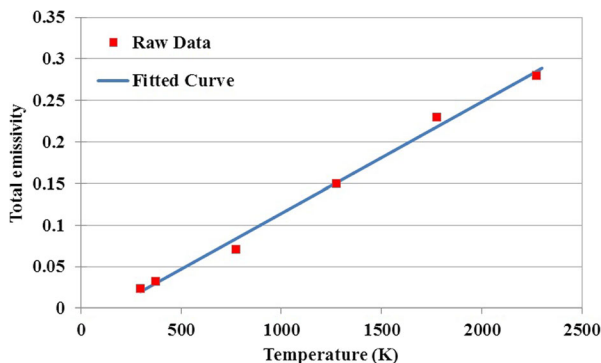


Fig. 4 Measured spectrum-average emissivity of tungsten against temperature and curve fitting [4]

From Fig. 5, the voltage-wave reflection coefficients can be expressed as [24]

$$\rho_1 = \frac{Z_S - Z_T}{Z_S + Z_T} \quad (9)$$

and

$$\rho_2 = \frac{Z_T - Z_S}{Z_S + Z_T} = -\rho_1 \quad (10)$$

where $Z_S \rightarrow \eta_1 = \sqrt{\frac{j\omega\mu}{\sigma + j\omega\epsilon}}$ is the intrinsic impedance of the glass; μ is the intrinsic permeability; σ is the intrinsic conductivity; ϵ is the intrinsic permittivity; and the termination impedance of the equivalent 2-port network $Z_T \rightarrow \eta_0$ is the intrinsic impedance of free space (i.e., the air dielectric).

The associated voltage-wave transmission coefficients are given by

$$\tau_1 = 1 + \rho_1 = \frac{2Z_S}{Z_S + Z_T} \quad (11)$$

and

$$\tau_2 = 1 + \rho_2 = \frac{2Z_T}{Z_S + Z_T} \quad (12)$$

Taking into account the infinite number of reflections between the air-glass and glass-air boundaries, using scattering (or S-)parameters, the overall forward voltage-wave transmission coefficient S_{21} and overall input voltage-wave reflection coefficient S_{11} can be represented as [24]

$$S_{21} = \tau_1 \cdot \left[\frac{e^{-\gamma T_h}}{1 - (e^{-\gamma T_h} \rho_1)^2} \right] \cdot \tau_2 \quad (13)$$

$$S_{11} = \rho_1 \cdot \left[\frac{1 - e^{-2\gamma T_h}}{1 - (e^{-\gamma T_h} \rho_1)^2} \right] \quad (14)$$

To calculate S_{21} and S_{11} , measured values for the index of refraction $\tilde{n}(\lambda) = n(\lambda) - jk(\lambda)$, where $n(\lambda)$ is the refractive index and $k(\lambda)$ is the extinction coefficient, for typical (soda lime silica) window glass was first needed [25]. The propagation constant through the glass γ is expressed as

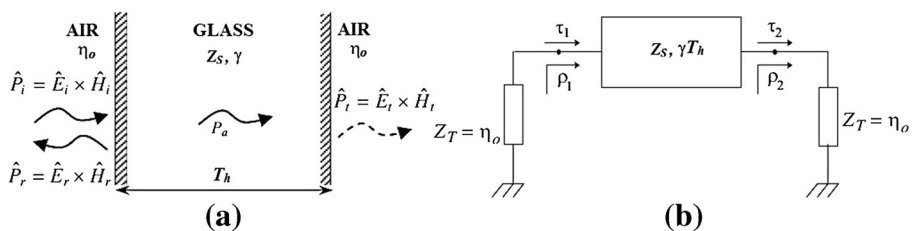


Fig. 5 Uniform plane-wave at normal incidence to the glass. (a) physical representation; (b) equivalent 2-port network model (adapted from [24])

$$\gamma = j \tilde{n}(\lambda) \cdot \frac{\omega}{c} = j 2\pi \frac{\tilde{n}(\lambda)}{\lambda} \quad (15)$$

At normal incidence, the intrinsic impedance of the glass is given by

$$\eta_1 = \frac{\eta_0}{\tilde{n}(\lambda)} \quad (16)$$

By applying (16) to (9)–(12), ρ_1 , ρ_2 , τ_1 and τ_2 can be obtained. As a result, S_{21} and S_{11} can then be calculated using (13) and (14). The overall power transmittance and reflectance are determined from $|S_{21}|^2$ and $|S_{11}|^2$, respectively, while power absorptance is given by $1 - |S_{11}|^2 - |S_{21}|^2$.

The Eiko 8666-40984 bulb has a measured glass envelope thickness of $\sim 300 \mu\text{m}$ at its sides and $\sim 400 \mu\text{m}$ at the top end. If an average value of $350 \mu\text{m}$ is taken for the glass envelope, the overall power transmittance $T_G(\lambda)$, reflectance and absorptance from 1 to 100 THz (assuming typical window glass at room temperature) is shown in Fig. 6. Here, $|\tau|^2 = |e^{-\alpha T_h}|^2$ and $|\rho|^2 = |\rho_1|^2$ and $1 - |\tau|^2 - |\rho|^2$ correspond to the power transmittance, reflectance and absorptance, respectively, without considering multiple reflections; these parameters are often plotted in the open literature as first-order approximations [25]. It can be seen in Fig. 6 that these first-order approximations are very accurate below ~ 65 THz ($4.6 \mu\text{m}$), where absorptance dominates.

It can also be seen from Fig. 6 that typical window glass can be considered opaque below ~ 60 THz ($5 \mu\text{m}$). For most conventional applications, this would only allow its use in its transparent region above ~ 70 THz ($4.3 \mu\text{m}$). However, for our ‘THz Torch’ applications, the high absorptance will contribute to the secondary source of radiation (due to the increase in outer surface temperature).

With the latter, to estimate $A_{\text{eff_filament}}$, the filament is assumed to be a uniform cylinder. Therefore, if CSA and l can be physically measured then the other can be extracted using the previously estimated value of $(CSA/l)_{\text{eff}}$. Using a scanning-electron microscope (SEM), the average value for the diameter of the filaments was measured to be $22.40 \mu\text{m}$, as shown in Fig. 7. Therefore, for the 5-bulb array configuration, the total effective radiating area is $A_{\text{filament}} = 12.73 \text{ mm}^2$ and $A_{\text{eff_filament}} = A_{\text{filament}}/2 = 6.37 \text{ mm}^2$.

2.5 Filament Thermal Time Constants

Filament thermal time constants are also important parameters for ‘THz Torch’ applications having transient behaviour in the electrical stimulus of the transducer (e.g., direct modulation);

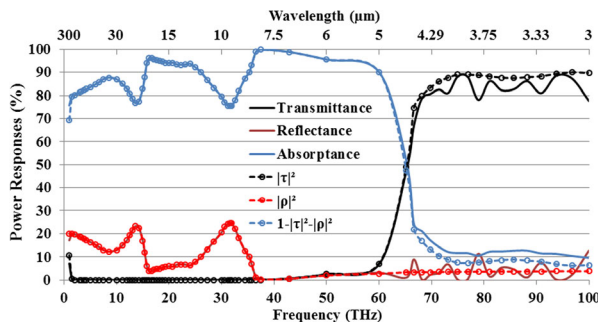


Fig. 6 Calculated power transmittance, reflectance and absorptance for $350 \mu\text{m}$ thick window glass at room temperature

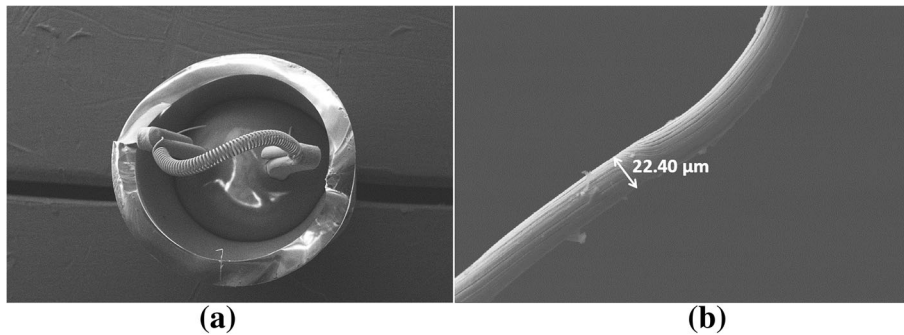


Fig. 7 SEM images of the Eiko 8666-40984 bulb's tungsten filament. (a) complete filament intact within the circular perimeter of the broken glass envelope; (b) close-in view of a section of filament

this will set fundamental limits on signalling rates. When the bulb is in the ON state, having a step response function, at its initial temperature $T(0)$, there is a large injection of current and the temperature of the filament increases. Since the resistivity of tungsten has a positive temperature coefficient, the instantaneous bulb resistance also increases; from its initial value of $R(T(0))$ until a steady-state value is reached, at thermal equilibrium, where the input power is exactly balanced out by all of the dissipative (i.e., heat transfer) loss mechanisms.

Fig. 8(a) shows the measured transient turn-ON current profile for a bias current of 44 mA. The transient temperature of the filament can be extracted, according to the measured bulb resistance, as shown in Fig. 8(b). A simple empirical curve fit can be applied to the instantaneous turn-ON filament temperature, as given by the following expression with less than 1.5 % error

$$T(t) = T(\infty) - \Delta T_{MAX} \cdot e^{-1.9995 t / \tau_H} \quad (17)$$

where t is the instantaneous heating time starting from the initial working temperature $T(0)$; $\Delta T_{MAX} = [T(\infty) - T(0)]$ is the maximum change in filament temperature; and $T(\infty)$ is the final steady-state working temperature in thermal equilibrium. With this example, $T(0) = 300$ K and $T(\infty) = 772$ K. The turn-ON thermal time constant was found experimentally to be $\tau_H = 645$ ms.

The cooling or turn-OFF thermal time constant τ_C is defined in a similar way to τ_H ; being the time taken to decrease from 90% to 10% of the temperature difference between the initial and final steady-state temperatures. Cooling of the hot filament is a relaxation process [14]. Therefore, τ_C is expected to be larger than τ_H . Using the measuring technique proposed in [4],

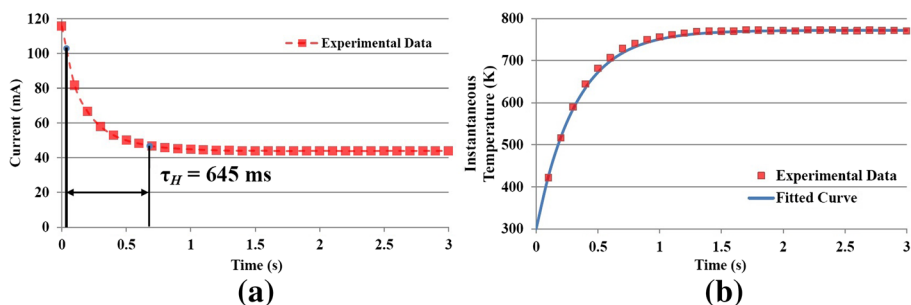


Fig. 8 Turn-ON responses giving the experimental values for instantaneous (a) current; (b) extracted filament temperature [4]

turn-OFF responses for instantaneous current and extracted filament temperature can be obtained, as shown in Fig. 9. A simple empirical curve fit can be applied to the instantaneous turn-OFF filament temperature, shown in Fig. 10(b), as given by the following expression with less than 3% error.

$$T(t) = T(\infty) + \Delta T_{MAX} \cdot e^{-2.415 \cdot t/\tau_c} \quad (18)$$

where t is the instantaneous cooling time from the initial working temperature $T(0)$; $\Delta T_{MAX} = [T(0) - T(\infty)]$ is the maximum change in filament temperature; and $T(\infty)$ is the final working temperature; with this example, $T(0) = 772$ K and $T(\infty) = 300$ K. The turn-OFF thermal time constant was found to be $\tau_c = 2,415$ ms. As expected, this value is much larger than τ_H . This severely limits the switching speed for the bulb and sets a practical limit on the data rate for on-off keying (OOK) digital modulation – although this is not an issue with applications that do not require high data rates.

3 Secondary Radiation Modelling

3.1 Band-limited Radiant Intensity from Secondary Radiation

Secondary radiation is defined as the radiation generated by the glass envelope due to its increased temperature. As seen in Fig. 6, below 65 THz (4.6 μm) the power transmittance through the glass envelope is poor and the secondary source of radiation dominates. The band-limited net radiant intensity from secondary radiation can be expressed as

$$I_{secondary}(T_{glass}) = A_{eff_glass} \cdot \int_{\lambda_2}^{\lambda_1} I_{NET}(\lambda, T_{glass}) \, d\lambda \quad [\text{W/sr}] \quad (19)$$

$$I_{NET}(\lambda, T_{glass}) = \varepsilon_{glass}(\lambda, T_{glass}) \cdot$$

$$\left(\frac{2h c^2}{\lambda^5} \cdot \frac{1}{e^{hc/\lambda k_B T_{glass}} - 1} - \frac{2h c^2}{\lambda^5} \cdot \frac{1}{e^{hc/\lambda k_B T_0} - 1} \right) \quad [\text{W/m}^2/\text{sr/m}] \quad (20)$$

where A_{eff_glass} [m^2] is the total effective radiating area for all the glass envelopes and $\varepsilon_{glass}(\lambda, T_{glass})$ is the emissivity of the glass envelope with an outer surface temperature T_{glass} . Here, we assume that $\varepsilon_{glass}(\lambda, T_{glass})$ does not change significantly as temperature increases from the ambient room temperature of 300 K to the highest elevated temperature of 366 K; this is a

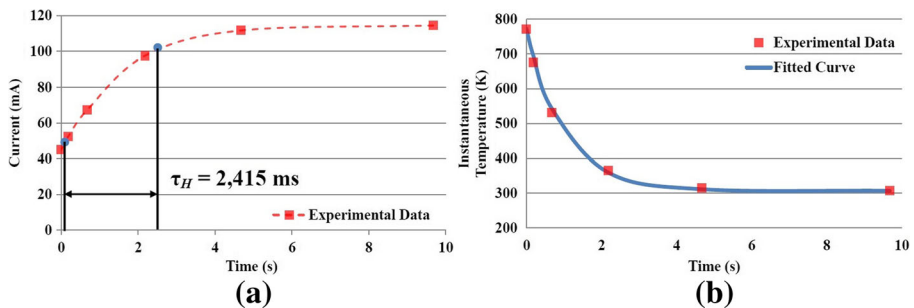


Fig. 9 Turn-OFF responses giving the experimental values for instantaneous (a) current; (b) extracted filament temperature [4]

reasonable assumption, as stated in [23]. Furthermore, according to Kirchhoff's law of thermal radiation, emissivity is equal to the power absorptance in thermal equilibrium. Therefore, the values for power absorptance shown in Fig. 6 can be used directly to represent the emissivity of the glass envelope $\varepsilon_{\text{glass}}(\lambda)$, which is now only wavelength-dependent.

With our particular 5-bulb array configuration, the radiant intensity from secondary radiation can be further separated out into two parts: the central higher temperature region and its surrounding lower temperature region, as shown in Fig. 10.

Therefore, (19) can be re-written as

$$I_{\text{secondary}}(T_{\text{glass}}) = I_{\text{glass}}(T_{\text{high}}) + I_{\text{glass}}(T_{\text{low}}) \quad [\text{W/sr}] \quad (21)$$

$$I_{\text{glass}}(T_{\text{high}}) = A_{\text{eff_glass_high}} \cdot \int_{\lambda^2}^{\lambda_1} I_{\text{NET}}(\lambda, T_{\text{high}}) d\lambda \quad [\text{W/sr}] \quad (22)$$

$$I_{\text{glass}}(T_{\text{low}}) = A_{\text{eff_glass_low}} \cdot \int_{\lambda^2}^{\lambda_1} I_{\text{NET}}(\lambda, T_{\text{low}}) d\lambda \quad [\text{W/sr}] \quad (23)$$

where T_{high} and T_{low} are the average temperatures for the high and low temperature regions, respectively; $A_{\text{eff_glass_high}} \approx D^2(1-\pi/4) = 1.45 \text{ mm}^2$ is the total effective radiating area of the higher temperature region for the five-bulb array; $A_{\text{eff_glass_low}} \approx 8\pi(D/2)^2 = 42.47 \text{ mm}^2$ is the total effective radiating area of the lower temperature region; and $D = 2.6 \text{ mm}$ is the diameter of the bulb's glass envelope.

The outer surface temperature of the glass envelope depends on the filament's emissivity, emitting area, temperature, position and shape. Instead of using complex thermodynamic modelling to simulate its outer surface temperature distribution, a more direct approach is to measure its temperature using a thermal camera. An experiment using a FLIR E60 thermal camera was performed. This camera uses an uncooled microbolometer focal plane array with 320×240 pixels. Note that the THz band-pass filter and associated aperture were removed, in order obtain the actual temperature distribution for the 5-bulb array.

Measured surface temperatures for the 5-bulb array, without bias and with bias currents from 44 mA to 80 mA, are shown in Fig. 11. For this experiment, room

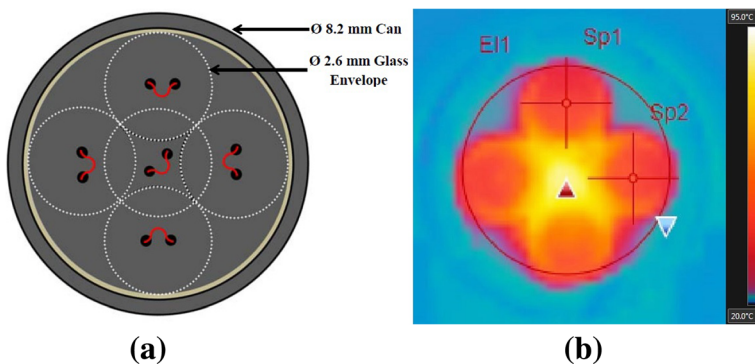


Fig. 10 Five-bulb array. (a) illustration of configuration, (b) measured surface temperature distribution (THz band-pass filter and aperture removed)

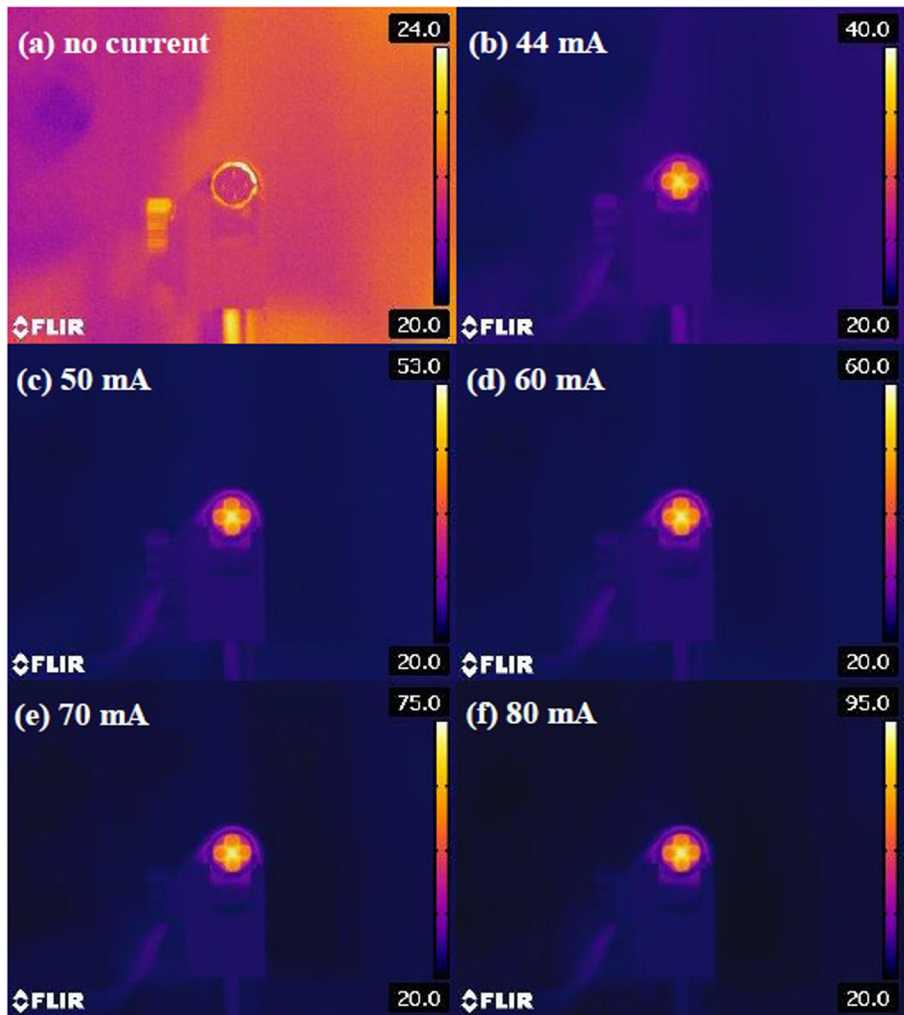


Fig. 11 Measured surface temperature distributions of the 5-bulb array as a function of bias current. (a) no current, (b) 44 mA, (c) 50 mA, (d) 60 mA, (e) 70 mA, (f) 80 mA

temperature was measured to be 21.5 °C (294.5 K). It can be seen that with this particular configuration, the central region of the source exhibits the highest temperatures.

The measured maximum and average temperatures for the 5-bulb array, as well as the temperature at the centre of the outer bulbs, for different bias currents, are given in Table 1. With reference to Fig. 10(b), the average temperature is measured within a circle (denoted by E11) and spot temperatures are given for two outer bulb centres (denoted by Sp1 and Sp2). The outer bulb centre values recorded in Table 1 represent the average values of Sp1 and Sp2, while the maximum temperature for the array is automatically captured by the camera within the selected area (located at the red triangle). After obtaining these temperature readings, the band-limited radiant intensity from secondary radiation can then be calculated using (21–23).

Table 1 Measured outer surface temperatures for the 5-bulb array at different bias currents

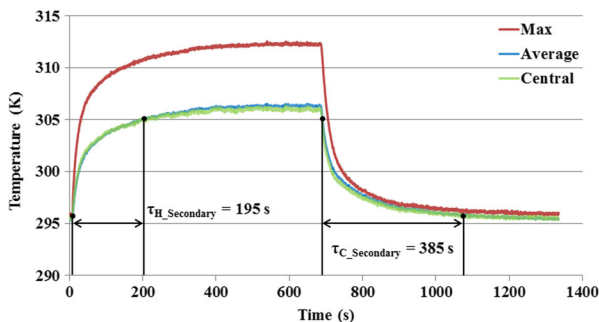
Bias Current (mA)	Measured Temperatures (K)		
	Array Maximum	Array Average	Outer Bulb Centre
0	294.5	294.5	294.5
40	308.9	304.0	303.9
44	312.3	306.3	306.0
50	318.9	310.6	310.4
55	325.3	315.3	315.0
60	331.8	319.9	319.4
65	338.9	324.9	324.4
70	346.9	330.9	330.4
75	355.7	337.3	336.7
80	366.1	344.9	344.2

3.2 Glass Envelope Thermal Time Constants

The instantaneous outer surface temperature of the glass envelopes can also be measured directly, giving the thermal time constants for the secondary radiation. The measured transient maximum and average temperatures for the 5-bulb array, as well as the temperature at the centre of the outer bulbs, for a 44 mA bias current, are shown in Fig. 12. It can be seen that the thermal time constants for the average temperature of the 5-bulb array is similar to that of the centre of the outer bulbs. Using the same definitions as those for the filament, the heating and cooling thermal time constants for the glass envelopes are measured to be 195 and 385 seconds, respectively, for a bias current of 44 mA. Therefore, the thermal time constants for the glass envelopes are between two and three orders of magnitude larger than those for the filament. This would create a fundamental limitation on the signalling rate if direct modulation is applied. However, this would not present a fundamental limit for ‘THz Torch’ applications if external modulators (e.g., programmable mechanical shutters or spatial light modulators) are employed.

4 Calculated and Measured Band-limited Output Radiated Power

The net spectral radiance for both primary and secondary radiation can be obtained by considering the spectrum-average emissivity of the filament $\overline{\varepsilon_{\text{filament}}(T_{\text{filament}})}$, power

**Fig. 12** Measured transient temperature for the 5-bulb array at a bias current of 44 mA

transmittance $T_G(\lambda)$ and emissivity $\varepsilon_{\text{glass}}(\lambda)$ of the glass envelope. Fig. 13 shows the calculated net spectral radiance from these two radiation mechanisms at a bias current of 44 mA. It is interesting to note that below ~ 50 THz ($6 \mu\text{m}$), secondary radiation dominates the output power; while primary radiation dominates above ~ 50 THz.

By inspection of Fig. 13, the contribution of the secondary radiation may seem insignificant, when compared to the primary radiation, given the low temperature. However, it will be shown that when the total effective radiating areas of $A_{\text{eff_filament}} = 6.37 \text{ mm}^2$ and $A_{\text{eff_glass}} = 43.92 \text{ mm}^2$ are taken into account for the filament and glass envelope, respectively, the resulting radiant intensities and band-limited output radiated powers are now of the same order of magnitude, for the bandwidth between 1 to 100 THz ($300 \mu\text{m}$ to $3 \mu\text{m}$), as shown in Fig. 14. As the bias current increases, the peak in spectral radiance increases in frequency, as dictated by (3). However, when compared to the secondary radiation mechanism, the output power from the primary radiation mechanism is more strongly coupled to changes in bias current.

The overall total radiant intensity, with contributions from both radiation mechanisms, is given by

$$I_{TX}(T) = I_{\text{primary}}(T_{\text{filament}}) + I_{\text{secondary}}(T_{\text{glass}}) \quad [\text{W/sr}] \quad (24)$$

By considering a projected solid angle of π , the total band-limited output radiated power is

$$P_{TX}(T) = \pi \cdot [I_{\text{primary}}(T_{\text{filament}}) + I_{\text{secondary}}(T_{\text{glass}})] \quad [\text{W}] \quad (25)$$

In order to verify this analysis, an experiment was performed to measure the total output radiated power from the 5-bulb array. The Ophir 10A thermal power sensor was used; this commercial power detector has a spectral range from 15 to 1,580 THz (i.e., from $20 \mu\text{m}$ to $0.19 \mu\text{m}$) [26]. The source and detector were positioned as close as possible to each other, so that all the generated power is captured by the large sensing element, having a diameter of 16 mm. In this experiment, there was no THz band-pass filter or apertures. With this experiment, the spectral range used for the calculation was chosen to be 15 to 300 THz (i.e., $20 \mu\text{m}$ to $1 \mu\text{m}$); the upper frequency limit is dictated by the available data for the complex index of refraction for glass [25]. However, this will not introduce any significant discrepancy, as most of the output radiated power (e.g. >99%) is between 15 and 300 THz, for all the temperatures considered here. The measured and calculated values for band-limited output radiated power are shown in Fig. 15. It can be seen that the measured results are in excellent agreement with

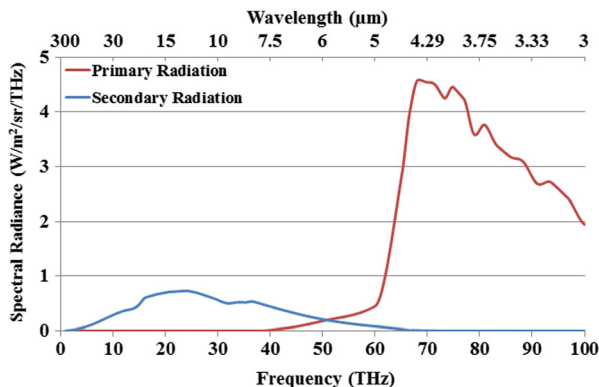


Fig. 13 Calculated net spectral radiance from both primary and secondary radiation at a bias current of 44 mA

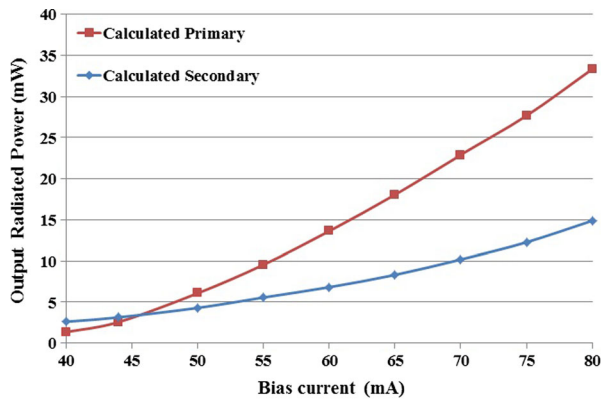


Fig. 14 Calculated band-limited (1–100 THz) output radiated power against bias current for the 5-bulb array

the calculated values, even though we have made many assumptions throughout, confirming the validity of our primary and secondary radiation modelling approaches.

5 Band-limited Output Radiated Power to Input DC Power Conversion Efficiency Calculations

In this section, the band-limited output radiated power and conversion efficiency for both single and multi-channel ‘THz Torch’ transmitters, employing the same 5-bulb array configuration described previously, can be calculated. The spectral range for the first proof-of-concept single-channel ‘THz Torch’ system was defined over the 25 to 50 THz (12 μm to 6 μm) octave bandwidth [1,3,4], while four non-overlapping spectral ranges for the 4-channel multiplexing systems are: 15 to 34 THz (20 μm to 8.8 μm) for Channel A; 42 to 57 THz (7.1 μm to 5.3 μm) for Channel B; 60 to 72 THz (5 μm to 4.2 μm) for Channel C; and 75 to 89 THz (4 μm to 3.4 μm) for Channel D [2,4–6].

Fig. 16 shows the calculated band-limited output radiated power levels. It can be seen that, for low bias currents, the single-channel and Channel A thermal sources can generate more band-limited output radiated power. The reason for this is that the spectral peak for the secondary radiation is at ~ 32 THz (9.4 μm), which is within the operation bands of these

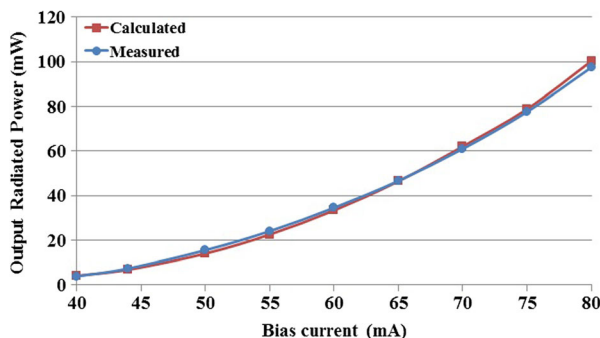


Fig. 15 Measured and calculated band-limited (15–300 THz) output radiated power against bias current for the 5-bulb array

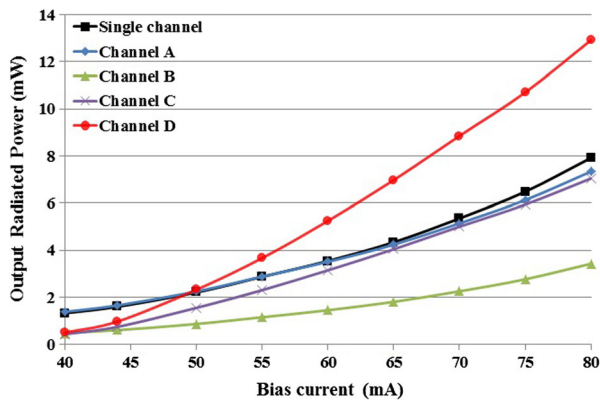


Fig. 16 Calculated band-limited output radiated power against bias current for single and multi-channel ‘THz Torch’ transmitters

two sources. While the spectral peak for the primary radiation is at ~ 80 THz (for a bias current of 44 mA), which lies within Channel D, the output power for Channel D is lower due to the smaller total effective radiating area. As the bias current increases, much more band-limited output radiated power will be generated within Channel D, surpassing the values from any other channel beyond a bias current of 50 mA. In the other extreme, Channel B is far from both primary and secondary radiation spectral peaks, and so its band-limited output radiated power is less than all the other channel sources. With multi-channel systems, different channels can have different quiescent DC bias currents, so that the band-limited output radiated power can be balanced between channels, optimizing the performance of complete frequency multiplexed systems.

The power conversion (or transducer) efficiency is defined as the ratio of band-limited output radiated power to input DC power. This efficiency has been calculated for different channels, as shown in Fig. 17. It has been previously estimated that for a 44 mA bias current, the filament has a working temperature of 772 K and that for a single bulb the corresponding resistance $R(772\text{ K}) = 17.02\ \Omega$. Therefore, the input DC power is $P_{DC} = I^2 R = 33\text{ mW}$. As a result, the conversion efficiency can be estimated to be $\sim 1\%$ for the single channel and

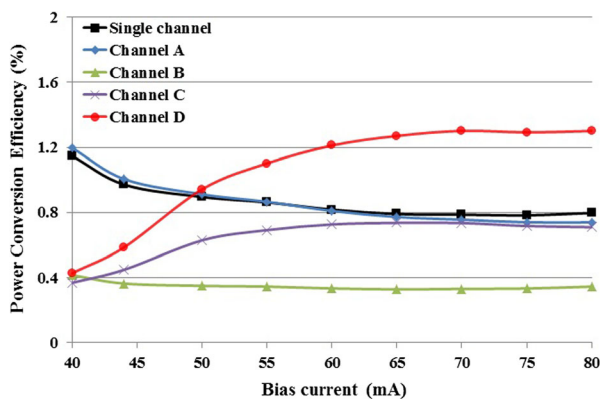


Fig. 17 Calculated power conversion efficiency against bias current for single and multi-channel ‘THz Torch’ transmitters

Channel A thermal sources and approximately half this value for the other channel sources at this bias point. It should be noted that the insertion loss of the THz band-pass filter and also spreading losses are not taken into account. As the bias current increases, the efficiency for the single channel and Channel A and B sources will decrease, as the spectral peak for the primary radiation moves higher in frequency, and more power is radiated above the spectral ranges of these channels. For this reason, Channel C and D sources show an increase in power conversion efficiency at higher bias currents.

6 Conclusions

The ‘THz Torch’ concept was recently proposed as a low cost means of establishing secure communications over short distances. In order to accurately characterize the thermal infrared transmitter and, in turn, predict the band-limited output radiated power for each channel, a detailed investigation of the associated radiation mechanisms has been given here for the first time. It is found that, with the use of incandescent light bulbs, the output radiated power has contributions from both the primary and secondary radiation sources. At a fixed bias current of 44 mA, these two radiation mechanism can generate similar band-limited (1–100 THz) output radiation power levels. In addition, the thermal time constants for both the tungsten filaments and glass envelopes have been investigated. For channels above ~ 70 THz ($4.3 \mu\text{m}$), where primary radiation dominates, the cooling thermal time constant of the filaments dictates switching speed. For channels below ~ 60 THz ($5 \mu\text{m}$), where secondary radiation dominates, the cooling thermal time constant of the glass envelope dictates switching speed; this is two to three orders of magnitude slower than those associated with the filaments.

Low cost near-infrared LEDs can provide even higher efficiency and switching speeds, but their output spectral frequency cannot be tuned. In contrast, the spectral peak of thermal sources can be continuously tuned over a vast spectral range, simply by changing the quiescent DC bias current.

The thermodynamic modelling approach reported here can accurately estimate the band-limited output radiated power of the thermal sources, and this has been verified by experimental results. Our modelling approach can serve as an invaluable tool for engineering solutions that can achieve optimal performances with both single and multi-channel ‘THz Torch’ systems. Moreover, the modelling methodology presented in this paper can be further extended to other incandescent light bulbs or more bespoke thermal sources, having different material systems, to predict the band-limited output power in the spectrum of interest.

Acknowledgements This work was partially supported by the China Scholarship Council (CSC).

Open Access This article is distributed under the terms of the Creative Commons Attribution License which permits any use, distribution, and reproduction in any medium, provided the original author(s) and the source are credited.

References

1. S. Lucyszyn, H. Lu and F. Hu, “Ultra-low cost THz short-range wireless link”, *IEEE International Microwave Workshop Series on Millimeter Wave Integrated Technologies*, Sitges, Spain, pp. 49–52, Sep. 2011.
2. F. Hu and S. Lucyszyn, “Ultra-low cost ubiquitous THz security systems”, *Proc. of the 25th Asia-Pacific Microwave Conference (APMC2011)*, Melbourne, Australia, pp. 60–62, Dec. 2011 (Invited).

3. F. Hu and S. Lucyszyn, “Improved ‘THz Torch’ technology for short-range wireless data transfer”, *IEEE International Wireless Symposium (IWS2013)*, Beijing, China, Apr. 2013.
4. F. Hu and S. Lucyszyn, “Emerging thermal infrared ‘THz Torch’ technology for low-cost security and defence applications”, Chapter 13, pp. 239–275, “*THz and Security Applications: Detectors, Sources and Associated Electronics for THz Applications*”, NATO Science for Peace and Security Series B: Physics and Biophysics, C. Corsi and F. Sizov (Editors), Springer Netherlands, Apr. 2014.
5. X. Liang, F. Hu, Y. Yan and S. Lucyszyn, “Secure thermal infrared communications using engineered blackbody radiation”, *Scientific Reports*, Nature Publishing Group, vol. 4, 5245, Jun. 2014.
6. F. Hu, J. Sun, H. E. Brindley, X. Liang and S. Lucyszyn, “Systems analysis for thermal infrared ‘THz Torch’ applications”, *Journal of Infrared, Millimeter, and Terahertz Waves*, Springer, 2015 (in press).
7. H. S. Just and C. F. Hanaman, Hungarian patent (No. 34541), Dec. 1904.
8. W. E. Forsythe and A. G. Worthing, “The properties of tungsten and the characteristics of tungsten lamps”, *Astrophysical Journal*, vol. 61, pp. 146–185, Apr. 1925.
9. B. T. Barnes and W. E. Forsythe, “Spectral radiant intensities of some tungsten filament incandescent lamps”, *Journal of the Optical Society of America*, vol. 26, no. 8, pp. 313–315, Aug. 1936.
10. R. H. Osborn, “Thermal conductivities of tungsten and molybdenum at incandescent temperatures”, *Journal of the Optical Society of America*, vol. 31, no. 6, pp. 428–432, Jun. 1941.
11. R. Raj and G. W. King, “Life prediction of tungsten filaments in incandescent lamps”, *Metallurgical Transactions A*, vol. 9, no. 7, pp. 941–946, Jul. 1978.
12. O. Horacek, “Properties and failure modes of incandescent tungsten filaments”, *IEE Proceedings A (Physical Science, Measurement and Instrumentation, Management and Education, Reviews)*, vol. 127, no. 3, pp. 134–141, Apr. 1980.
13. D. C. Agrawal, H. S. Leff, and V. J. Menon, “Efficiency and efficacy of incandescent lamps”, *American Journal of Physics*, vol. 64, no. 5, pp. 649–654, May 1996.
14. T. Durakiewicz and S. Hala, “Thermal relaxation of hot filaments”, *Journal of Vacuum Science & Technology A: Vacuum, Surfaces, and Films*, vol. 17, no. 3, pp. 1071–1074, Jun. 1999.
15. J. Wei, H. Zhu, D. Wu and B. Wei, “Carbon nanotube filaments in household light bulbs”, *Applied Physics Letters*, vol. 84, no. 24, pp. 4869–4871, Jun. 2004.
16. A. Y. Vorobyev, V. S. Makin, and C. Guo, “Brighter Light Sources from Black Metal: Significant Increase in Emission Efficiency of Incandescent Light Sources”, *Physical Review Letters*, vol. 102, no. 23, pp. 204301–1–204301–4, Jun. 2009.
17. T. Matsumoto and M. Tomita, “Modified blackbody radiation spectrum of a selective emitter with application to incandescent light source design”, *Optics Express*, vol. 18, no. S2, pp. A192–A200, Jun. 2010.
18. J.-J. Greffet, R. Carminati, K. Joulain, J.-P. Mulet, S. Mainguy and Y. Chen, “Coherent emission of light by thermal sources”, *Nature*, vol. 416, no. 6876, pp. 61–64, Mar. 2002.
19. F. Kusunoki, T. Kohama, T. Hiroshima, S. Fukumoto, J. Takahara and T. Kobayashi, “Narrow-band thermal radiation with low directivity by resonant modes inside tungsten microcavities”, *Japanese Journal of Applied Physics*, vol. 43, no. 8A, pp. 5253–5258, 2004.
20. S. Tay, A. Kropachev, I. E. Araci, T. Skotheim, R. A. Norwood and N. Peyghambarian, “Plasmonic thermal IR emitters based on nanoamorphous carbon”, *Applied Physics Letters*, vol. 94, no. 7, pp. 071113–1–071113–3, 2009.
21. X. Liu, T. Tyler, T. Starr, A. F. Starr, N. M. Jokerst, and W. J. Padilla, “Taming the blackbody with infrared metamaterials as selective thermal emitters”, *Physical Review Letters*, vol. 107, no. 4, pp. 045901–1–045901–4, Jul. 2011.
22. T. Inoue, M. D. Zoysa, T. Asano and S. Noda, “Realization of dynamic thermal emission control”, *Nature Materials*, vol. 13, no. 10, pp. 928–931, 2014.
23. D. R. Lide (Ed.), *CRC Handbook of Chemistry and Physics*, CRC Press, 77th Edition, 1996.
24. S. Lucyszyn and Y. Zhou, “Characterising room temperature THz metal shielding using the engineering approach”, *PIER Journal*, vol. 103, pp. 17–31, Apr. 2010.
25. M. Rubin, “Optical properties of soda lime silica glasses”, *Solar Energy Materials*, vol. 12, no. 4, pp. 275–288, Sep. 1985.
26. Ophir Optonics Solutions Ltd, “Datasheet: low power thermal sensors”, [Online]. Available: http://www.ophiropt.com/laser-measurement/sites/default/files/10A_30A-BB-18_L30A-10MM_50%28150%29A-BB-26.pdf